

X-RAY SPECTRAL ANALYSIS OF *YOHKOH* BRAGG CRYSTAL SPECTROMETER DATA ON A 1992 SEPTEMBER 6 FLARE: THE BLUESHIFT COMPONENT AND ION ABUNDANCES

TAKAKO KATO,¹ TOMOKO FUJIWARA,² AND YOICHIRO HANAOKA³

Received 1996 January 23; accepted 1997 August 14

ABSTRACT

We have studied the time evolution of Bragg crystal spectrometer spectra of He-like Ca XIX and Fe XXV ions observed by the *Yohkoh* satellite for a solar flare on 1992 September 6 at 05:05 UT (M2.4 class). Electron temperatures are derived through a fit of synthetic spectra to the observed Ca XIX and Fe XXV spectra using new evaluated atomic data. Ion density ratios derived from spectra without assuming ionization equilibrium show a time-dependent, nonequilibrium ionization. The shift from equilibrium values indicates an ionizing plasma. For the first time the emission measures are derived from the spectra without assuming ionization equilibrium and solar abundances. Apparent ion temperatures are derived from the line widths of Ca XIX spectra. In the rising phase a blueshifted component is separated from the main component of the Ca XIX spectra. The time variation of these parameters are compared with hard X-rays, soft X-rays, and radio measurements. In the preheating phase, a moderate increase of the amount of thermal plasma is observed with turbulence indicated by the line width. The time evolution of the blueshifted component coincides with that of a burst in hard X-rays and microwaves which are produced by high-energy, nonthermal electrons.

Subject headings: Sun: abundances — Sun: flares — Sun: X-rays, gamma rays

1. INTRODUCTION

Bragg crystal spectrometer (BCS) experiments on board the *Yohkoh* satellite launched in 1991 August have been providing X-ray spectra of He-like Ca XIX, S XV, and Fe XXV ions (Lang et al. 1992; Doschek et al. 1992; Culhane et al. 1992). The *Yohkoh* BCS is about 1 order of magnitude more sensitive than previous X-ray flare spectrometers and is able to measure the early stages of a flare in detail.

Many spectroscopic measurements of solar flares have been performed by BCS on the *P78-1*, *SMM*, and *Hinode* satellites, and the high-resolution X-ray spectra give information about electron temperature, electron density, dynamic motion, and ion ratios. Doschek (1990) reviewed soft X-ray spectroscopy of solar flares and discussed questions about the temperature of coronal flare plasma, electron density measurements, nonequilibrium processes, and relative element abundances. Many of these questions are still unresolved. As Doschek pointed out, the atomic physics plays a crucial role for this kind of plasma diagnostics. For example, the intensity ratio of the inner shell satellite line (*q*) to the resonance line often gives an apparent excess from ionization equilibrium for the Li-like ion density (e.g., Doschek et al. 1980; Antonucci et al. 1987). It has been said that this discrepancy may be a question about the atomic data. For another example, the electron temperature is usually derived mainly from the intensity ratios of the dielectronic satellite lines and the resonance line. However, these lines have a contamination of other lines such as inner shell satellite lines for the dielectronic satellite lines and a recombination contribution in the resonance line. Then using different atomic data will change the values of the derived temperatures. The aim of this paper is to

analyze the spectra with reliable atomic data and an atomic model for line intensities to derive reliable plasma parameters from BCS spectra. For this purpose we employ atomic data for He-like Ca and Fe ions evaluated by Itikawa et al. (1995) for ionization, recombination, and excitation rate coefficients and by Kato et al. (1997) for the satellite lines.

In this paper we present a detailed spectral analysis of time-dependent BCS data for the solar flare on 1992 September 6 at 05:05 UT (M2.4 class) using evaluated atomic data without assumption of ionization equilibrium. We have fitted the spectra with fit parameters of electron temperature, ion temperature, and ion abundances as a function of time. The time history of ion density ratios is derived, and the results deviate from values corresponding to ionization equilibrium. Usually the emission measure is derived from the line intensity, with ion abundances based on an assumption of ionization equilibrium. We have derived the emission measure without assumption of the ionization equilibrium for the first time. This method gives a larger emission measure of Fe ions than that assuming ionization equilibrium. The emission measure of Ca and Fe ions are almost the same values, although the assumption of ionization equilibrium would give smaller values for Fe ions than Ca ions by a factor of 3 as given in Doschek et al. (1996).

In the initial phase before the rising phase, the Ca XIX and Fe XXV X-ray spectra indicate a high-temperature thermal plasma. In the rising phase a very broad spectral shape of the Ca XIX resonance line is observed. We separate a blueshift component from the main component in the rising phase and derive the ion temperatures and the emission measures. These parameters are compared with hard X-rays, microwaves, and soft X-rays. An increase of the electron temperature from 15 to 24 MK (10^6 K) in the rising phase is obtained from the Fe XXV spectra. These measurements during the rising phase give important information for the flare model.

¹ National Institute for Fusion Science, Oroshi, Toki, 509-52, Japan.

² Department of Education, Aichi University of Education, Kariya, 448, Japan.

³ Nobeyama Radio Observatory, National Astronomical Observatory, Nobeyama, Nagano 384-13, Japan.

Yohkoh contains a soft X-ray telescope (SXT) and a hard X-ray telescope (HXT). The SXT produces soft X-ray images of the Sun with high time and spatial resolutions with various filters (Tsuneta et al. 1991). The HXT provides hard X-ray data for four energy bands with time resolution of 0.5 s (Kosugi et al. 1991). This flare was observed with SXT and the hard HXT on board *Yohkoh* and by the Nobeyama radioheliograph. The radioheliograph, which is a microwave interferometer, observes the Sun at 17 GHz in both right- and left-hand circular polarizations with a field of view which covers the entire Sun, with spatial and temporal resolutions of 12" and 1 s (Nakajima et al. 1994). The correlation of the blueshifted component measured by BCS and HXT have been studied extensively in previous *Yohkoh* measurement (e.g. Bentley et al. 1994; Doschek et al. 1996; Doschek et al. 1994; Culhane et al. 1994). We have compared the time evolution of the emission measure of the blueshifted component and HXT radio emission and radio polarization and also find a correlation.

2. ATOMIC DATA AND MODEL

We have constructed a code to calculate synthetic spectra of He-like ions including satellite lines. This model is based on the collisional radiative (CR) model of He-like ions (Fujimoto & Kato 1984) for the line intensities emitted from singly excited states. This model includes the recombination contribution from H-like ions as well as excitation from He-like ions for an arbitrary H-like/He-like ion abundance ratio. The dielectronic satellite lines as well as the inner shell satellite lines are added to the spectra. We have also included the continuum emission (free-free emission, free-

bound emission; Mewe et al. 1985, 1986) in the spectra. For the spectral fit, we did not assume ionization equilibrium for the ion ratios, and the best spectral fit is obtained with nonequilibrium ion abundance ratios.

The excitation, the inner shell excitation, ionization, and recombination rate coefficients have been evaluated by Itikawa et al. (1995) for *Yohkoh* BCS spectra. We have used these atomic data in our program and in Figures 1, 4, 5, 9, and 10 below. For the dielectronic satellite lines the wavelengths and intensities calculated by Safronova given in Kato et al. (1997) are used. The wavelengths of the excitation lines and the satellite lines by Safronova with MZ code and by Cornille with AUTLSJ code were compared in Kato et al. (1997). The intensities of the satellite lines are also compared in this paper. The temperatures derived using these two different atomic data sets (MZ and AUTLSJ) differ by about 10%. For the inner shell excitation rate coefficients, data by Bely-Dubau et al. (1982) for Li-like Fe ions and Itikawa et al. (1995) for Li-like Ca ions are used, respectively. For the inner shell excitation cross sections of Be-, B-, and C-like Fe ions, the data by Safronova given in Kato et al. (1997) are used.

An example of the Fe spectrum is shown in Figure 1. For Fe xxv spectra, the dielectronic satellite lines for $n = 3$ have wavelengths near the resonance line and have intensities much lower than those of the $n = 2$ satellite lines (j, k) as shown in Figure 1, although for low ionized ions such as S xv the intensities of dielectronic satellite lines for $n = 3$ are almost the same as those of $n = 2$ satellite lines. The inner shell satellite lines of Li-like, Be-like, and B-like ions are shown by dotted curves in Figure 1.

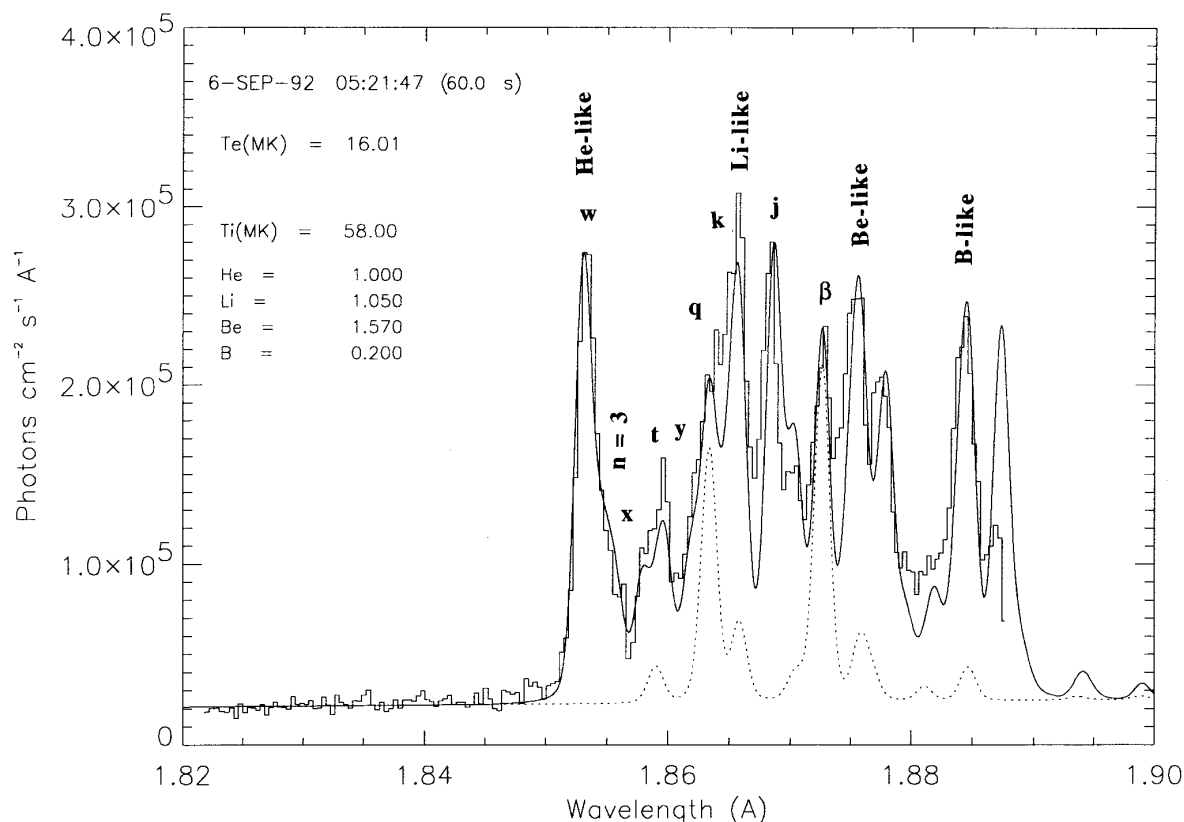


FIG. 1.—Fe xxv spectra in decay phase at 05:21:47 UT (start time) on 1997 September 6 flares. Dotted lines show line intensities due to inner shell excitation of Li-like (q), Be-like (β), and B-like (I4) ions. T_e is the derived electron temperature in MK; T_i is the apparent ion temperature; He, Li, Be, and B indicate the ion density ratios of He-, Li-, Be-, and B-like Fe ions to the He-like Fe ion.

3. BCS SPECTRAL ANALYSIS

The *Yohkoh* BCS consists of four Bragg crystal spectrometers that cover narrow-wavelength ranges including the resonance lines and associated satellite lines of H-like Fe xxvi (1.7636–1.8044 Å), He-like Fe xxv (1.8298–1.8942 Å), He-like Ca xix (3.1631–3.1912 Å), and He-like S xv (5.0160–5.1143 Å). The spectrometers view the entire Sun. These spectral ranges assume an on-axis flaring source. The actual wavelength ranges observed vary with the north-south location of the event, which is due to the orientation of the Bragg crystals with respect to the Sun (Mariska 1994). Therefore, the observed wavelengths depend on the position of the flares and are generally shifted from the absolute values. The radiation diffracted by the crystal is detected by two position-sensitive proportional counters. The effective sensitive areas are 0.114 and 0.152 cm² for Fe xxv and Ca xix detectors, respectively (Sterling 1996, private communication), and these areas can be used to compute the photon numbers from the spectra given in Figures 4 and 5 below.

A Voigt line profile is used for the spectral fit. A Voigt profile has Lorentz and Gaussian parameters. The Lorentz parameter for Fe xxv and Ca xix is taken from the crystal rocking curve, 0.000206 and 0.0003889 Å, respectively (A. Fludra 1994, private communication). The Gaussian component originates in plasma Doppler broadening and is time dependent. The small additional broadening which is due to the noise of the electronics is assumed to have a Gaussian shape. The prelaunch FWHM values which are due to noise are 0.000526 and 0.000294 Å, respectively (A. Fludra 1994, private communication). However, for Fe xxv spectra we obtain much higher ion temperature (e.g., 70 MK) than electron temperature (e.g., 21 MK). We consider this to be due to the instrumental resolution rather than to ion motion.

From the fit of the synthetic spectra to the observed spectra we can obtain several plasma parameters as described in the following subsections. We did not assume ionization equilibrium in our fitting procedure.

The four kinds of free parameters used in fitting procedure are as follows:

1. Electron temperature (T_e) is obtained from the intensity ratio of the satellite lines to the resonance line.
2. Apparent ion temperature (T_i) is obtained from the line widths.
3. Ion density ratios of Li-like, Be-like, and B-like ions to the He-like ion are obtained from the line intensity ratios. For Fe ions, the ion ratio $n(\text{Li-like})/n(\text{He-like})$, $n(\text{Be-like})/n(\text{He-like})$, and $n(\text{B-like})/n(\text{He-like})$ are the free parameters, where $n(\text{He-like})$ is the density of He-like ion. From Ca spectra we cannot obtain the Ca ion density ratio since the wavelength range is too short.
4. Density ratio of the He-like ions to the hydrogen, $n(\text{He-like})/n(\text{H})$ is obtained from the intensity ratio of the resonance line to the continuum, where $n(\text{H})$ is the density of hydrogen.

In this section we explain the methods to derive these parameters. The results are given in the next section.

3.1. Electron Temperature (T_e)

We have derived the electron temperature mainly from the intensity ratio of the satellite lines and the resonance line. For Fe xxv spectra, spectral range is rather wide from

the He-like resonance line (1.8500 Å) to the B-like satellite lines (1.885 Å), as shown in Figure 1. For the northern hemisphere flares, we can measure C-like satellite lines. The temperature is derived mainly from the resonance line (w) and the dielectronic satellite lines (j). for Ca xix spectra, the resolution is much better than Fe spectra, and the spectral range is short from resonance line (3.1771 Å) to the intercombination line (3.1927 Å). The electron temperature is mainly decided by the intensity ratio of the resonance line and the $n = 3$ dielectronic satellite lines near the resonance line.

3.2. Ion Temperature (T_i) and Blueshifted Component

The ion temperature is derived mainly from the broadening of the resonance line. In the rising phase, Ca xix spectra show much larger broadening than expected from the electron temperature, and the average wavelength of the resonance line is shifted to the blue side compared to that in the decay phase. We therefore fit the broadening with two components: a main component and a blueshifted component as a standard procedure (e.g., Doschek et al. 1993). The wavelength of the main component is fixed as that in the decay phase through all the time. The blueshifted component is determined to fit the rest of the main component. Then the wavelength shift, the apparent ion temperature, and the intensity are obtained. We derive the relative velocity of the blueshifted component from the shift of the wavelength to the main component.

3.3. Ion Abundance

3.3.1. I_w/I_c

From the intensity ratio of the resonance line (I_w) to the continuum (I_c), the ion abundance ratio $n(\text{He-like ion})/n(\text{H})$ can be derived using the electron temperature obtained from the spectra, where $n(\text{He-like ion})$ and $n(\text{H})$ are the densities of He-like ion and hydrogen, respectively. Usually the abundance of the element Z , $n(Z)/n(\text{H})$, is obtained from I_w/I_c assuming ionization equilibrium

$$I_w/I_c = (\epsilon_w/\epsilon_c) [n(\text{He-like})/n(Z)]_{\text{eq}} [n(Z)/n(\text{H})], \quad (1)$$

where ϵ_w and ϵ_c are the emissivities of the resonance line and the continuum. However, we do not use this assumption and derive the density ratio of $n(\text{He-like})/n(\text{H})$ from the following formula,

$$I_w/I_c = (\epsilon_w/\epsilon_c) [n(\text{He-like})/n(\text{H})]. \quad (2)$$

3.3.2. I_w/I_s

From the intensity ratio of the resonance line I_w to the inner shell satellite lines I_s ($1s^2 2s^n 2p^m - 1s 2s^n 2p^{m+1}$), the ion ratios can be derived. From Fe spectra we can derive the ion ratios of $n(\text{Li-like})$, $n(\text{Be-like})$, and $n(\text{B-like})$ to $n(\text{He-like})$. We did not assume ionization equilibrium to determine the ion abundances. All the ion density ratios are obtained from spectral fit.

3.4. Volume Emission Measure (EM)

The observed line intensity I_w is written as

$$\begin{aligned} I_w &= \epsilon_w n(\text{He-like ion}) n_e V / (4\pi r^2) \text{ photons cm}^{-2} \text{ s}^{-1} \text{ sr}^{-1} \\ &= \epsilon_w [n(\text{He-like ion})/n(Z)] [n(Z)/n(\text{H})] [n(\text{H})/n_e] n_e^2 V / (4\pi r^2) \end{aligned} \quad (3)$$

$$= \epsilon_w [n(\text{He-like ion})/n(\text{H})] [n(\text{H})/n_e] n_e^2 V / (4\pi r^2), \quad (4)$$

where ϵ_w is the emissivity ($\text{cm}^3 \text{s}^{-1}$) of the line w , n_e is the electron density, $n(Z)$ and $n(\text{H})$ are the densities of the element of Z and hydrogen, V is the volume where the line is emitted, and r is the distance from Earth to the Sun.

The emission measure $n_e^2 V$ is usually derived assuming ionization equilibrium for $n(\text{He-like ion})/n(Z)$ and element abundance for $n(Z)/n(\text{H})$ to be the solar abundance from equation (3). But we have derived the emission measure from equation (4) using the density ratio $n(\text{He-like ion})/n(\text{H})$ derived directly from the observed intensity ratio I_w/I_c without assuming ionization equilibrium and solar abundance.

4. TIME EVOLUTION OF THE PLASMA PARAMETERS

The time evolution of the integrated flux of the three different BCS spectra is shown in Figure 2a, together with hard X-ray counting rate and microwave (17 GHz) brightness in Figures 2b and 2c. The fluxes of Fe xxv, hard X-ray, and microwaves show similar time behavior while those of Ca xix and S xv are delayed. The dashed line in Figure 2c is the degree of circular polarization measured in microwave (17 GHz). Figure 3 shows the images in soft X-rays, 17 GHz microwaves, and white light. Figures 3a–3c show the soft X-ray images for the initial phase, the rising phase, and maximum phase, respectively. Figures 3d–3f give a comparison between the flare loop in soft X-rays (contour) and a 17 GHz image in the initial phase, a white light image, and a map of longitudinal B (magnetic field), respectively. We can see that one footpoint of the flare loop coincides with the sunspot where the magnetic field is strong. Furthermore, this footpoint coincides with the radio source.

Time-dependent spectra are classified into four phases as follows. We show the spectra of each phase in Figures 4 and 5 for Ca xix and Fe xxv ions, respectively. The accumula-

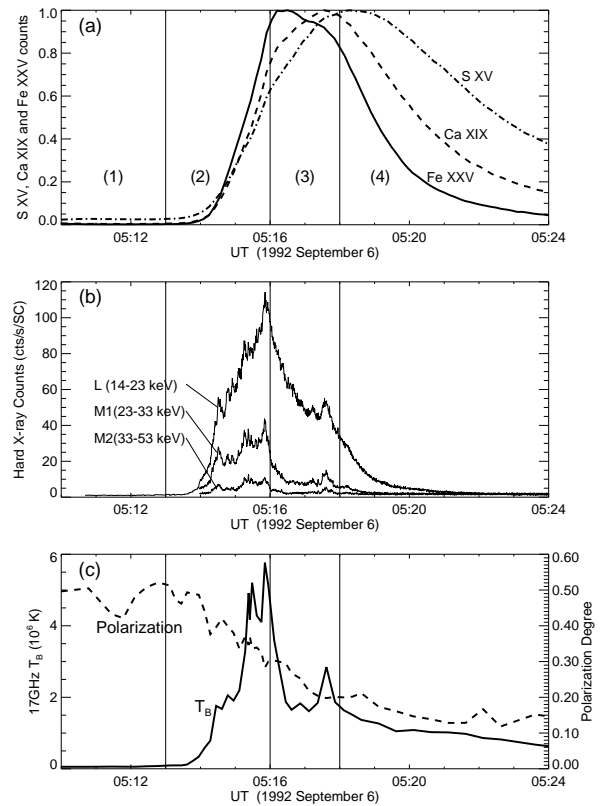


FIG. 2.—(a) Time evolution of the integrated flux of Fe xxv, Ca xix, and S xv BCS spectra. The values of flux are normalized by the maximum flux value of each ion. The maximum flux is 8746, 11,358, and 20,202 counts s^{-1} for Fe xxv, Ca xix, and S xv, respectively. (b) Time evolution of hard X-ray counts of the L, M1, and M2 bands of the HXT. (c) Time evolution of the brightness temperature and the degree of polarization at 17 GHz of the brightest point in the radio pictures.

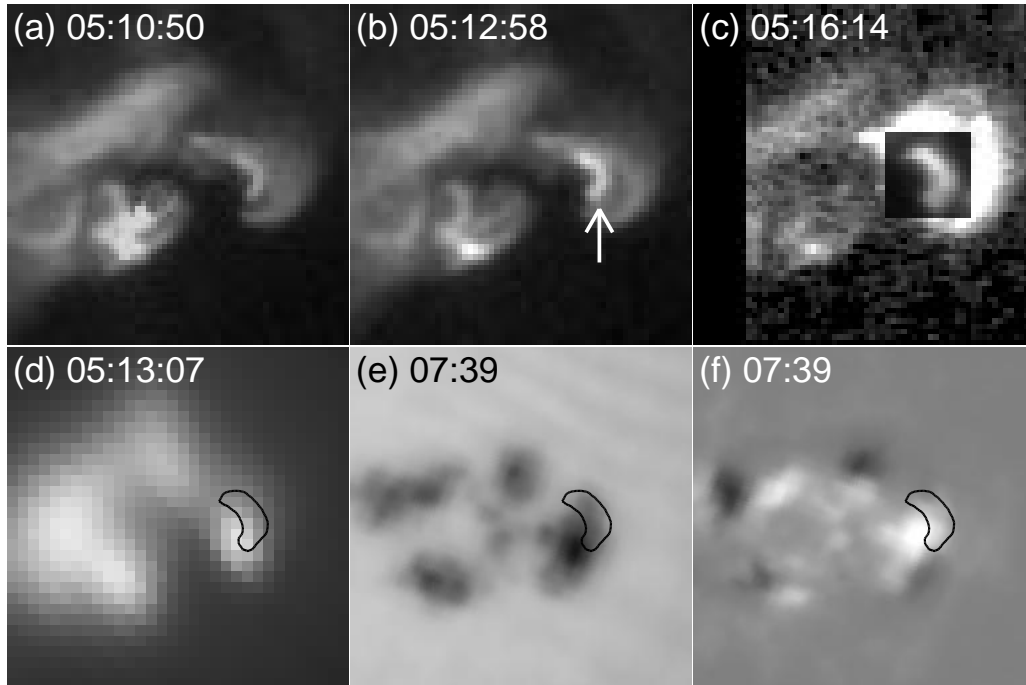


FIG. 3.—Images of the solar flare on 1992 September 6, 05:05 UT. Solar north is to the top, and each panel has a field of view of 2.6×2.6 . (a)–(c) Solar flare images taken by the SXT. An arrow in (b) shows the main flare loop. The three pictures are displayed in the same brightness scale except the region of the main flare loop in (c), which is extremely bright. (d) A radio picture at 17 GHz. (e), (f) White light map and magnetogram of longitudinal B taken with the flare telescope at Mitaka. In the magnetogram the north and south polarities are displayed in white and black, respectively. The position of the main flare loop observed in soft X-rays is shown as a contour in (d)–(f). The images (e) and (f) were taken 2.5 hr after the flare.

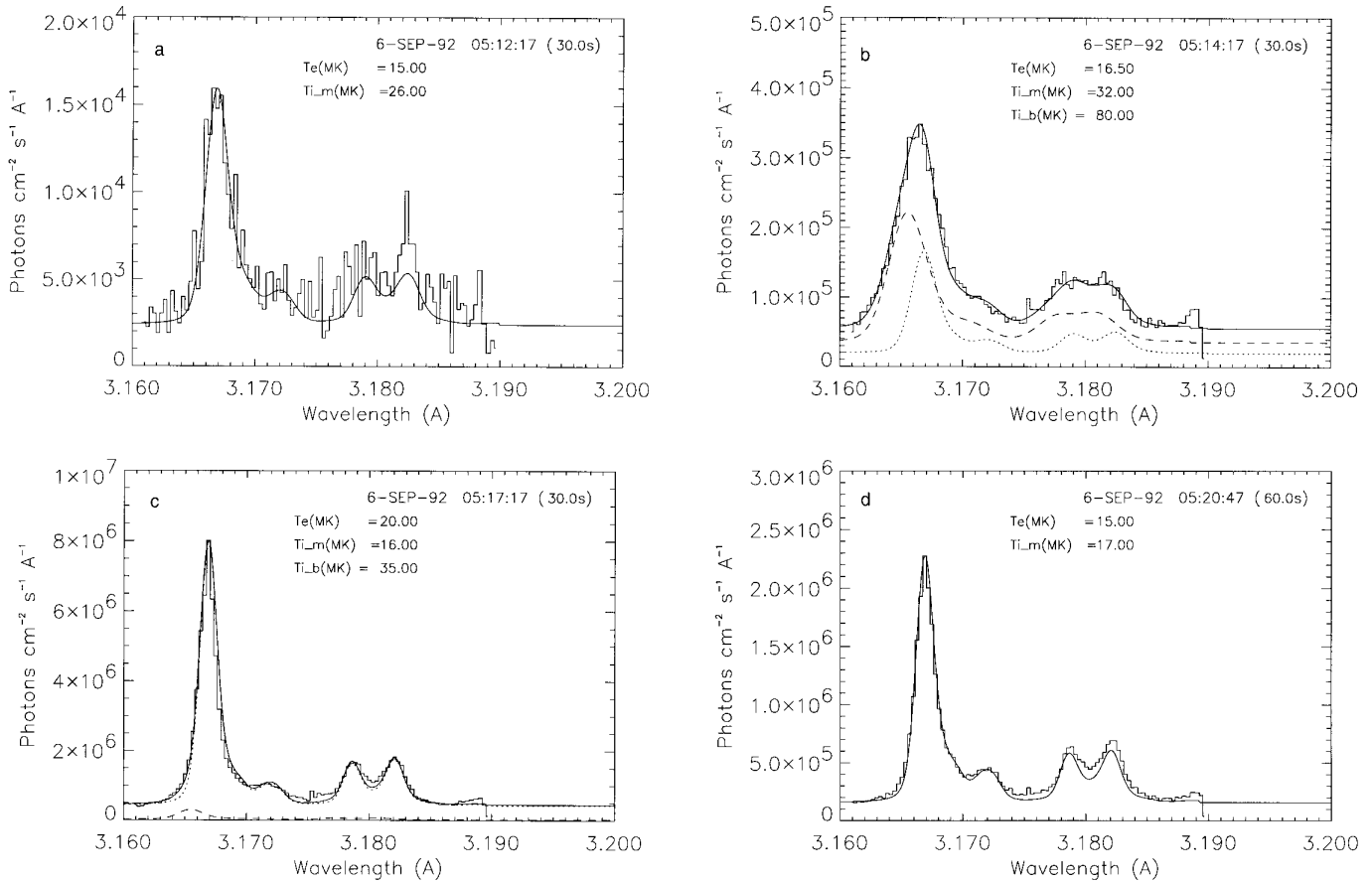


FIG. 4.—Time evolution of BCS Ca XIX spectra. (a) Initial phase, (b) rising phase, (c) maximum phase, and (d) decay phase. The dotted and dashed lines indicate the main and the blueshift component, respectively. Since the observed wavelengths depend on the position of the flare on the Sun, they are generally shifted from the absolute values. The intensity (photons $\text{cm}^{-2} \text{s}^{-1} \text{\AA}^{-1}$) is obtained for the accumulation time indicated in the figures. The observed photon numbers can be obtained from the effective sensitive area and accumulation time. T_{im} and T_{ib} are the apparent ion temperature of main and blueshifted component, respectively.

tion times are usually 30 and 60 s for Ca XIX and Fe XXV, respectively. They are indicated in the figures.

1. *Initial phase* (05:10–05:13).—Counting rates are very low, almost constant, and increase gradually with time. The Ca XIX spectra show the line broadening of about 26 MK, larger than the electron temperature which is around 15 MK. From the Fe XXV spectra during 05:12:00–14:00, $T_e = 15$ MK is obtained, although the statistics are bad. The emission measure in the initial phase is about $2 \times 10^{47} \text{ cm}^{-3}$ from Fe XXV and Ca XIX. A gradual increase of soft X-rays and microwaves is also observed during this period.

2. *Rising phase* (05:13–05:16).—The counting rate begins to increase very rapidly. The flux of Fe XXV increases rapidly compared to that of S XV. The flux of Fe XXV begins to decrease when the flux of Ca and S are still increasing as shown in Figure 2a. This phenomenon has been observed very often in previous measurements. The electron temperatures increase following the increase of the counting rate. Line widths become broader than those in the initial phase, and the blueshifted component becomes obvious at the beginning of the rising phase. The hard X-rays, which are generally considered to be produced by high-energy electrons, begin to increase rapidly almost at the same time. The hard X-ray counts reach their maximum value when the emission measure of the blueshifted component reaches its maximum (Figure 8 below). The time behavior of microwave brightness is similar to that of hard X-rays after the

rising phase, and the polarization of the radio source decreases down to 20% until the maximum phase.

3. *Maximum phase* (05:16–05:18).—The counting rates of Ca XIX and Fe XXV reach a maximum, as do the electron temperatures. The line widths of the main component become narrow, indicating no turbulence. The blueshifted component is still seen, but the ratio to the main component is small (about 20%). Hard X-ray and radio emission begin to decrease in the beginning of this phase.

4. *Decay phase* (05:18–05:25).—The electron temperature decreases from 25 to 12 MK as well as the counting rates. The ion temperature of Ca spectra becomes a little larger than in the maximum phase to be around 20 MK.

4.1. Electron Temperature (T_e)

The time evolution of the electron temperatures T_e derived from each ion are shown in Figure 6. The maximum electron temperature from Fe XXV, $T_e(\text{Fe})$ is 23 MK at about 1 minute before the maximum of $T_e(\text{Ca})$ and 1–2 minutes before the period when the counting rates are maximum. The value $T_e(\text{Fe})$ is higher than $T_e(\text{Ca})$ in the rising phase. The values of $T_e(\text{Fe})$ and $T_e(\text{Ca})$ coincide in the maximum phase. The electron temperatures derived from the SXT data with Be and A1 12 μm filters are much lower than those from BCS data.

Doschek et al. (1993) analyzed *Yohkoh* data in the rising phase of an M1.9 flare on 1992 January 5 and derived the

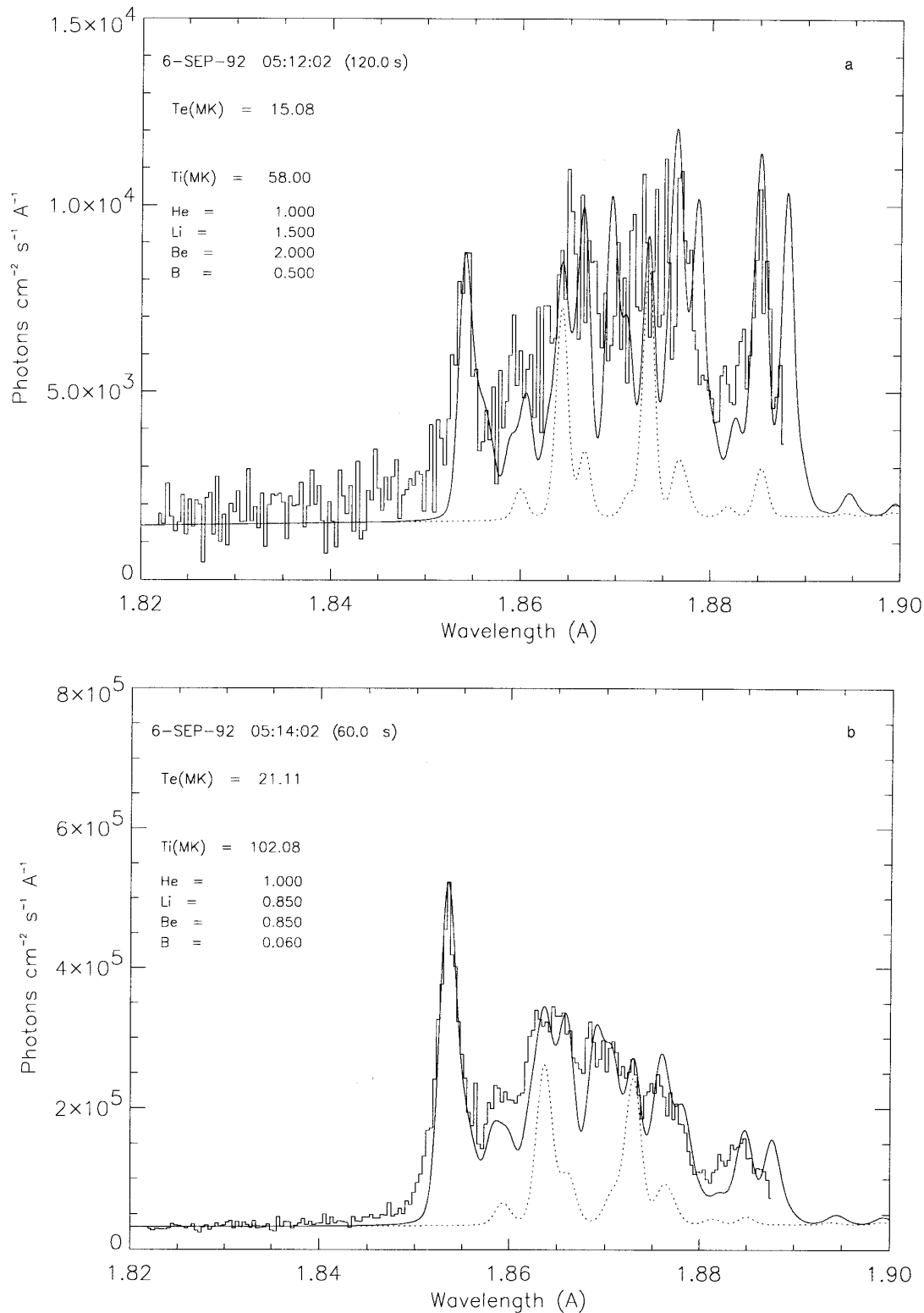


FIG. 5.—Time evolution of BCS Fe xxv spectra. (a) Initial phase, (b) rising phase, (c) maximum phase, and (d) decay phase. The dotted curve indicates the contribution of the inner shell excitation of Li, Be, and B-like ions.

time variation of T_e . The maximum temperature they found for $T_e(\text{Fe})$ was 20 MK. In our case the highest temperature is about 23 MK from Fe spectra. Tanaka (1986) gives temperatures from Fe xxv and Fe xxvi for some intense flares from *Hinotori*. The maximum temperature derived from Fe xxvi is higher than that from Fe xxv. The temperature given in Tanaka (1986) in the decay phase is nearly 20 MK,

which is higher than the 15 MK seen in our case. Doschek (1990) summarized the temperature results from previous satellites in his overview; he found $T_e(\text{Ca})$ is always lower than $T_e(\text{Fe})$, and this differs from our results. The temperatures for two different ions in the decay phase are almost the same in our case, as shown in Figure 6. Recently Sterling et al. (1994) derived the temperature from the ratio

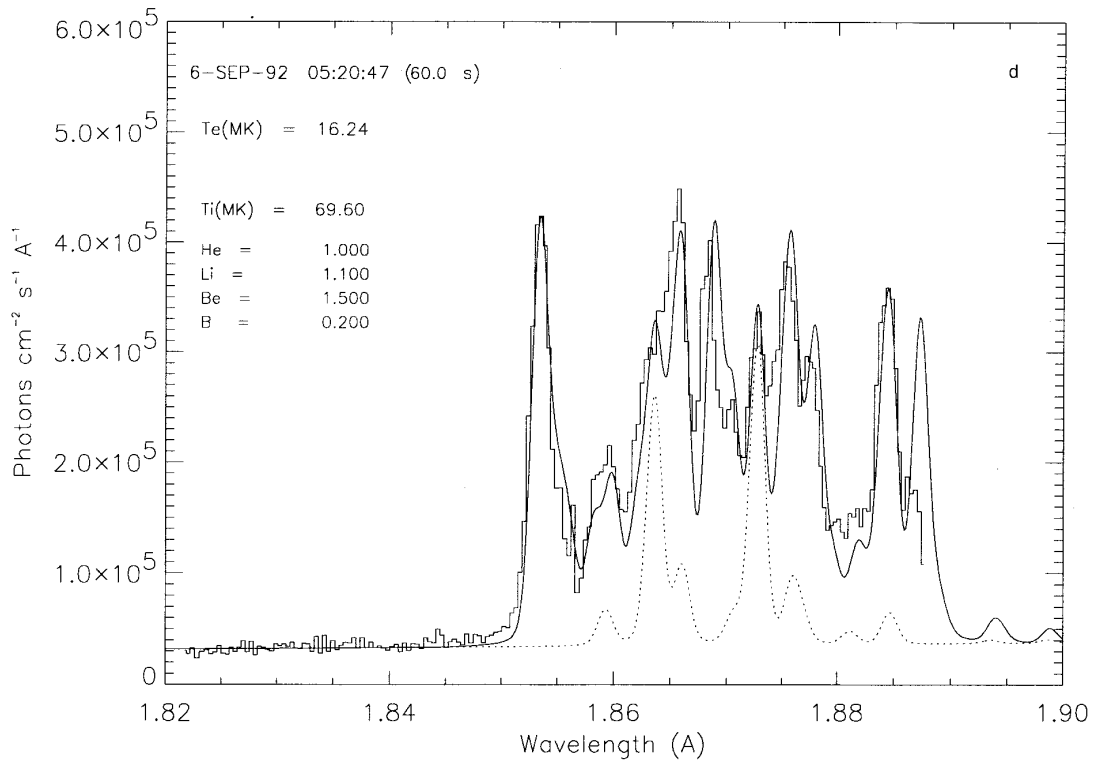
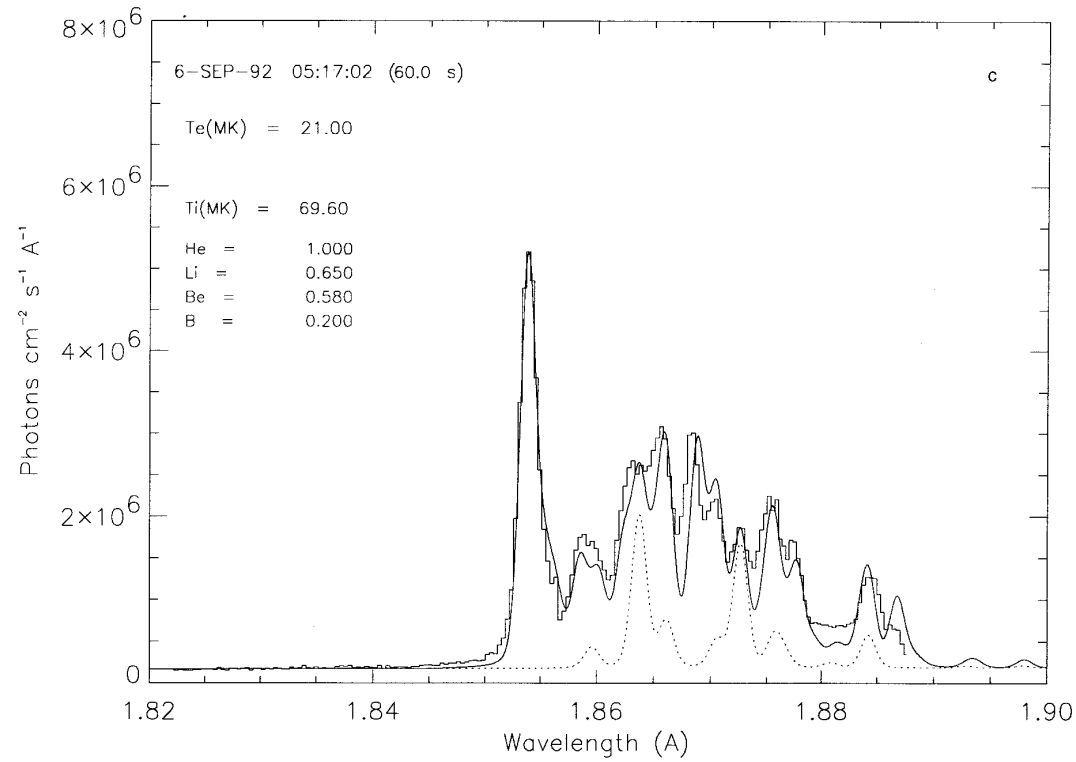


FIG. 5—Continued

of intensities of the Fe xxv and Ca xix resonance lines and compared to Fe xxv temperature. Their derived temperatures cover our values.

4.2. Ion Temperature (T_i)

Ca xix spectra in the initial and rising phase show broad line width, which indicates more than two blueshifted components (Doschek et al. 1992) as shown in Figure 4.

The average central wavelength of the resonance line in the rising phase is shifted to the blue side compared to those in the decay phase. During the rising phase the apparent ion temperature of the main component is about 32 MK, whereas that of the blueshifted component is around 80 MK, which indicates turbulence of about 130 km s^{-1} and 230 km s^{-1} , respectively. The relative velocity of the two components is derived to be 130 km s^{-1} from the wave-

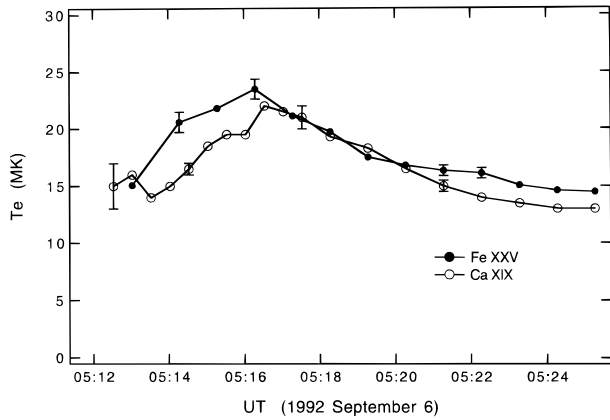


FIG. 6.—Time evolution of the electron temperature derived from BCS Fe XXV and Ca XIX spectra.

length shift of $1.4 \times 10^{-3} \text{ \AA}$. The relative velocity goes down to 100 km s^{-1} toward the maximum phase, as shown in Figure 7. Relative velocities of the blueshifted component in Doschek et al. (1993) are 250 km s^{-1} in the beginning of the rising phase and decay, down to 100 km s^{-1} after 5 minutes. The values in Doschek et al. (1996) are $300\text{--}150 \text{ km s}^{-1}$. Their values are higher than our values.

The apparent ion temperatures derived from the main component of Ca XIX are shown in Figure 7 together with the electron temperature as a function of time. The ion temperature of about 20 MK from Ca XIX, $T_i(\text{Ca})$, in the initial phase indicates that the turbulence (100 km s^{-1}) begins before the increase of the X-ray flux. In the initial phase the blueshifted component has not appeared yet. The line broadening including the main and blueshifted component reaches a maximum value at the beginning of the rising phase (05:14) and decreases toward the maximum phase. The ion temperature decreases from 05:14 toward the maximum phase and reaches a value close to the electron temperature in the decay phase. This indicates that thermalization occurs in the maximum phase.

$T_i(\text{Ca})$ goes down and reaches a value around 12 MK, lower than the electron temperatures $T_e = 20 \text{ MK}$. We consider this to be due to the narrowing of the spectral shape

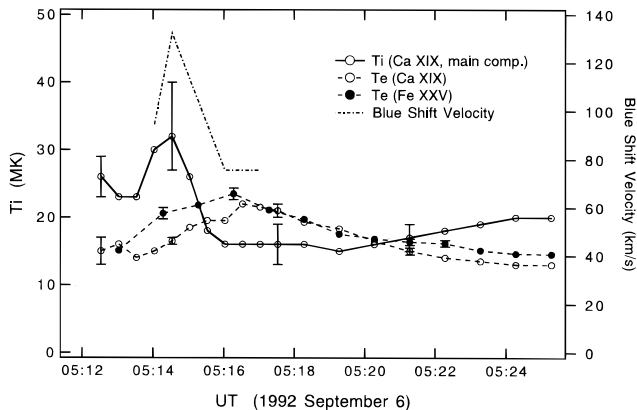


FIG. 7.—Time evolution of the apparent ion temperature T_i from Ca XIX spectra. The ion temperature of the main component is shown. The electron temperatures are also plotted for comparison. The T_i values during 05:16–05:20 are affected by narrowing as the result of high counting rate saturation. The relative velocity of the blueshift component is also shown.

by saturation effect caused by the high counting rate. The ion temperature from 05:16 to 05:20 is not a real value.

The derived $T_i(\text{Fe})$ is always much larger than $T_i(\text{Ca})$. The typical value of $T_i(\text{Fe})$ is about 70 MK in the decay phase in our analysis. Comparing to the spectra of Fe ions obtained by Hinotori (Tanaka 1986), we think that the derived high values of $T_i(\text{Fe})$ from Yohkoh are too high and are mainly due to limited spectral resolution. Actually the $T_i(\text{Fe})$ values obtained by Hinotori from flares in X class (Tanaka 1986) are smaller than our values. Therefore we do not show the values of $T_i(\text{Fe})$ in Figure 7.

4.3. Emission Measure (EM)

The volume emission measure $n_e^2 V$ is derived without assuming ionization equilibrium and solar abundance as explained in § 3.3. The derived emission measures (EM) from two different spectra of Fe and Ca are shown in Figure 8. The values of EM(Ca) and EM(Fe) agree well with each other in all the phases including the rising phase. When ionization equilibrium is assumed, the derived $[\text{EM}(\text{Fe})]_{\text{eq}}$ from equation (3) is generally smaller than $[\text{EM}(\text{Ca})]_{\text{eq}}$ by more than a factor of 2. This agreement is evidence for nonequilibrium ionization in solar flares, as will be seen in the next section on abundances. In Figure 8, the emission measures $[\text{EM}]_{\text{eq}}$ derived from the line intensity assuming the ionization equilibrium are also plotted for Fe and Ca. The solar abundances for $n(\text{Fe})/n(\text{H})$ and $n(\text{Ca})/n(\text{H})$ are taken to be 5×10^{-5} and 5×10^{-6} , respectively, to derive $[\text{EM}]_{\text{eq}}$. The emission measure derived in Doschek et al. (1993) gives smaller values for Fe than Ca and S because they assumed ionization equilibrium. Their emission measure for Ca is about half that of S.

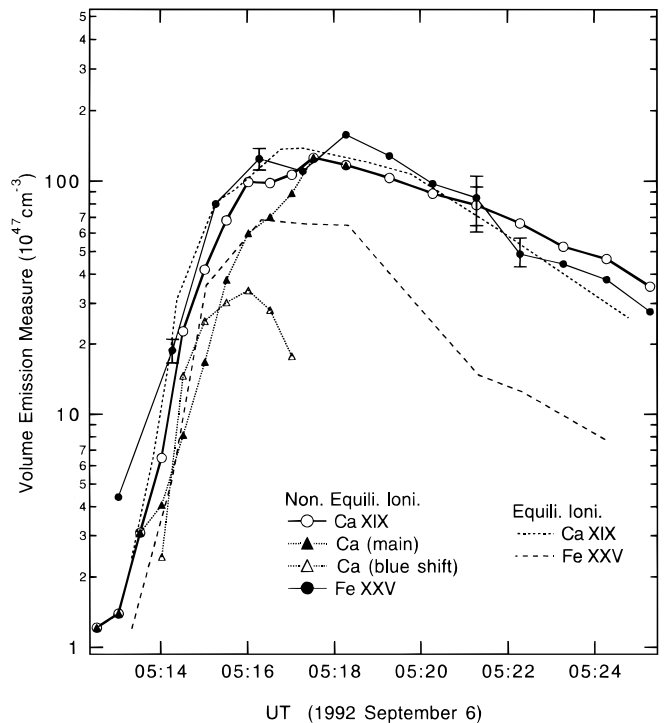


FIG. 8.—Time evolution of the emission measures derived from Fe XXV and Ca XIX spectra. Solid and dotted lines with symbols are those obtained using eq. (3) without assuming ionization equilibrium, whereas the dashed and dot-dashed lines without symbols are those obtained with eq. (4) using the ionization equilibrium.

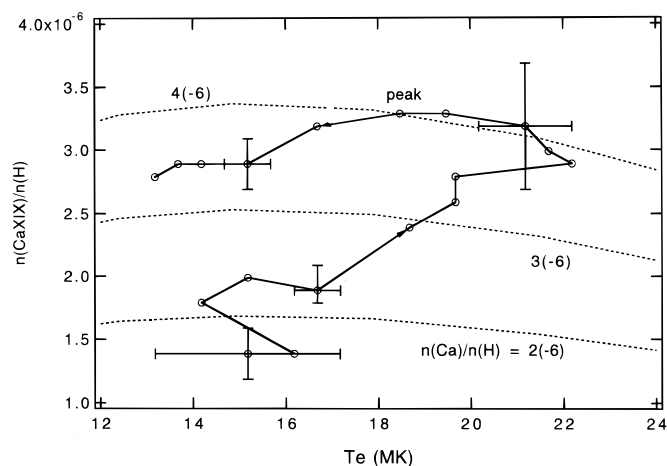


FIG. 9a

FIG. 9.—Density ratio $n(\text{He-like ion})/n(\text{H atom})$ as a function of the electron temperature. The values in the initial phase are always smaller than those in the later phase. (a) $n(\text{Ca XIX})/n(\text{H})$, (b) $n(\text{Fe XXV})/n(\text{H})$.

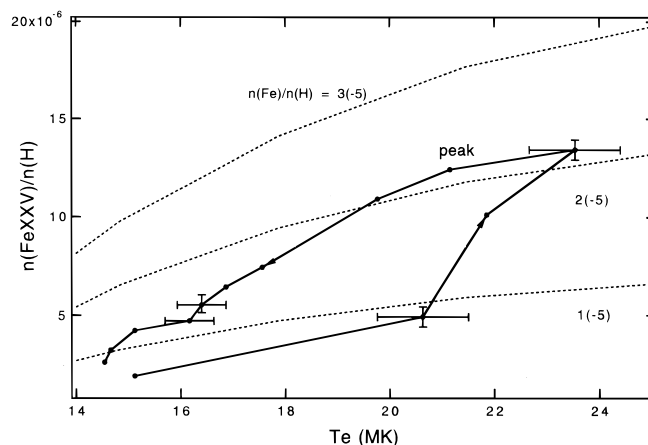


FIG. 9b

The emission measure of the blueshifted component reaches its maximum before the maximum phase, and only the main component increases afterward as shown in Figure 8. The ratio of the blueshifted component to the main component is about 0.2–0.3 at the beginning and increases to more than unity. But this ratio decreases from the end of the rising phase, and the blueshifted component disappears in the main component after the maximum phase as shown in Figure 8. This behavior is similar to hard X-ray and radio emission. The ratio of the blueshifted component to the main component in Doschek et al. (1993) decreases toward the maximum phase, which is opposite to our case. Doschek

et al. (1996) discussed the dynamics of four soft X-ray flares and showed the time-dependent emission measure of the main component and the blueshifted component. The blueshifted component lasts more than 4 minutes for two flares, although it continues only 2 minutes in our case. Fludra et al. (1989) analyzed the Ca XIX and Fe XXV spectra from SMM satellite with a two-component model. The emission measures of the blueshifted component increase gradually over 10 minutes and then decay. They are smaller than those of the main component. This behavior is also different from our case.

4.4. Abundances

We have derived the density ratio $n(\text{He-like})/n(\text{H})$ from the line to continuum I_w/I_c ratio as mentioned in § 3.3.1. For the continuum intensity we have to know the spurious background radiation from other sources, such as scattering within the spectrometers, the electronic noise, etc. In order to evaluate the contribution of the spurious background in the continuum emission, we compared the observed continuum intensity I_c of two spectra. The intensities of $I_c(\text{Fe XXV}, \sim 1.84 \text{ \AA})$ and $I_c(\text{Ca XIX}, \sim 3.18 \text{ \AA})$ are generally on the line of the same temperature in the maximum phase and decay phase. Therefore, the spurious background can be neglected in the maximum and decay phase.

In our analysis the continuum flux is not independent of the derived T_e and EM because we derive the density ratio $n(\text{He-like})/n(\text{H})$ from the ratio of the continuum to the line intensities and use this ratio to derive the EM from equation (4). This method is different from the ordinary one which derives EM and continuum independently. That is the original point of our analysis.

The derived density ratios $n(\text{Fe XXV})/n(\text{H atom})$ and $n(\text{Ca XIX})/n(\text{H atom})$ are plotted in Figure 9 as a function of the electron temperature. The dotted lines in Figure 9 indicate the ionization equilibrium values; $[n(\text{He-like})/n(\text{H})]_{\text{eq}} = [n(\text{He-like})/n(\text{Z})]_{\text{eq}} [n(\text{Z})/n(\text{H})]$, where $n(\text{Z})/n(\text{H})$ is solar abundance of the element Z. The values of abundance $n(\text{Z})/n(\text{H})$ are written in the figures. The derived values in the rising phase and the decay phase are not the same for the same temperature. This indicates nonequilibrium ionization, as will be discussed in § 5. From Figure 9 we can say

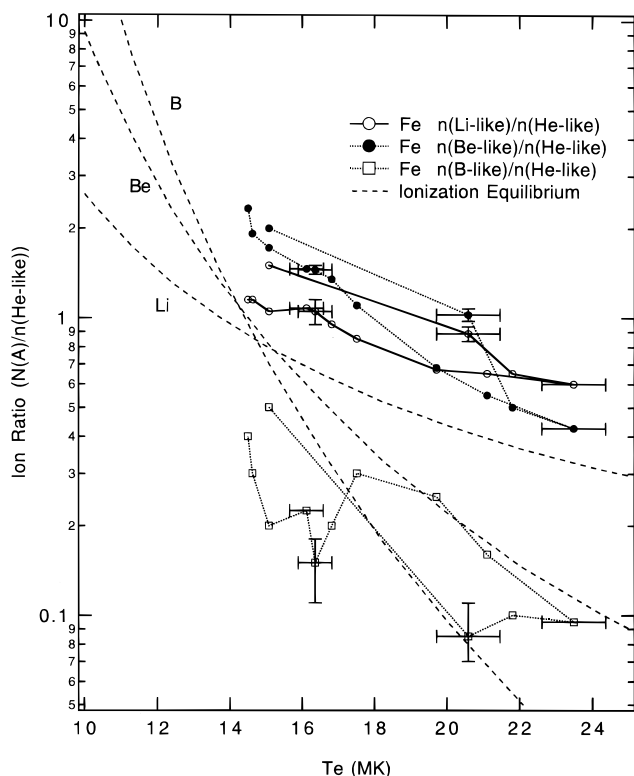


FIG. 10.—Ion density ratios of Fe ions as a function of T_e . The ion density ratios in the initial phase are always larger than those in the decay phase for Li-like and Be-like ions.

that the lower limits of $n(\text{Ca})/n(\text{H})$ and $n(\text{Fe})/n(\text{H})$ are 4×10^{-6} and 2.2×10^{-5} , respectively.

The ion density ratios $n(\text{Fe xxiv})/n(\text{Fe xxv})$, $n(\text{Fe xxiii})/n(\text{Fe xxv})$, and $n(\text{Fe xxii})/n(\text{Fe xxv})$ are derived from the line intensity ratios of the inner shell satellite lines to the resonance line. The derived values are plotted as a function of electron temperatures for Fe ion in Figure 10. These values are derived only from the line intensity ratios without continuum emission. The ratios in ionization equilibrium are plotted as dotted lines. More detailed discussion will be given in § 5.

The fit was done by eye, and the error bars shown in figures are obtained by changing the parameters during the fit. The fitting errors for T_e , T_i , and ion ratio are about 5%, 20%, and 8%. The uncertainty of emission measure is about 20%.

5. ION ABUNDANCE AND SOLAR ABUNDANCE

The density ratios $n(\text{Ca xix})/n(\text{H})$ and $n(\text{Fe xxv})/n(\text{H})$ in the rising and decay phases at the same temperature are not the same value as shown in Figure 9. The values in the rising phase are always smaller than those in the decay phase. The value $n(\text{He-like})/n(\text{H})$ increases in the rising phase and reaches the maximum near the temperature maximum. The period when the flux reaches the maximum is indicated as “peak” in the figures. Sylwester et al. (1984) interpreted this variation to be due to abundance variation during the flare. We do not consider these variations as being due to abundance variation but rather as due to variation of the ionization degree. The dashed curves in Figure 9 show the ratios $n(\text{He-like})/n(\text{H})$ in ionization equilibrium assuming the solar abundances indicated in the figures. If we assume the solar abundance $n(\text{Ca})/n(\text{H}) = 4 \times 10^{-6}$, and $n(\text{Fe})/n(\text{H}) = 2 \times 10^{-5}$, the derived values are in ionization equilibrium only for the period 05:16:17–05:17:47 and 05:15:47–05:17:47 for Ca and Fe ions, respectively. In the decay phase the ratios again deviate from ionization equilibrium. This phenomenon would not occur in a closed system. Because the recombination time is less than 10 s, the ion abundances should be always in ionization equilibrium in the decay phase. Therefore it is considered that there is some flow and/or escape of the highly ionized ions. Another possible explanation is the effect of high-energy electrons. We will investigate these effects in another paper.

If we assume ionization equilibrium at the maximum phase when T_e reaches the maximum value, the abundances obtained are $n(\text{Ca})/n(\text{H}) = 4 \times 10^{-6}$ and $n(\text{Fe})/n(\text{H}) = 2 \times 10^{-5}$ which can be compared to the solar abundances $n(\text{Ca})/n(\text{H}) = 3 \times 10^{-6}$ and $n(\text{Fe})/n(\text{H}) = 4 \times 10^{-5}$ given by Meyer (1985). Fludra et al. (1993) derived abundances from Yohkoh BCS. Their values of $n(\text{Ca})/n(\text{H})$ are in the range $2.5\text{--}4.5 \times 10^{-6}$ which overlap the lower range of Ca abundances from SMM data.

The ion abundance ratios $n(\text{Fe xxiv})/n(\text{Fe xxv})$, $n(\text{Fe xxiii})/n(\text{Fe xxv})$, and $n(\text{Fe xxii})/n(\text{Fe xxv})$ derived from Fe xxv spectra are always larger than those in ionization equilibrium as shown in Figure 10. This indicates that the ionization balance is not in ionization equilibrium in solar flares. We had the same results for the M1.3 flare on 1992 January 21 (Kato et al. 1993). Antonucci et al. (1987) obtained similar results from SMM BCS Fe spectral data. They interpreted the deviation as being due to the error of the ionization rate coefficients. Similar results for the devi-

ation from ionization equilibrium for the q line of Li-like ions are given in many papers (e.g., Doschek & Feldman 1981; Doschek et al. 1993). In order to clarify the atomic data problem, we did a careful evaluation of atomic data relating to our spectral analysis (Itikawa et al. 1995; Kato et al. 1997) and used these evaluated data for our analysis. We believe that the deviation from the equilibrium ion ratio is due to nonequilibrium ionization. The plasma is considered to be an ionizing plasma ($T_e > T_z$, where T_z is the ionization temperature where the ion is the most abundant in ionization equilibrium) even in the decay phase.

The emission measures derived from Ca and Fe spectra by equation (4) without assuming ionization equilibrium give similar values as shown in Figure 8. The emission measure $[\text{EM}(\text{Fe})]_{\text{eq}}$ from Fe spectra by equation (3) assuming ionization equilibrium is more than a factor of 3 smaller than that without assuming ionization equilibrium as shown by a dashed line in Figure 8. This indicates also nonequilibrium ionization for Fe ions.

6. SUMMARY AND DISCUSSION

From Ca xix and Fe xxv spectra, SXT data and radio emission, there is evidence that the thermal plasma around 15 MK is created in the initial phase (05:11–05:13) before the rapid increase of X-ray flux. The Ca xix spectra shows an ion temperature of 23 MK, higher than the electron temperature 15 MK (Fig. 7) because of the turbulence. In the rising phase the blueshifted component in Ca spectra begins to increase at around 05:13:30, and hard X-rays and microwaves begin to increase rapidly almost at the same period. The blueshifted component increases until the maximum phase. The hard X-ray counts reach the maximum value when the blueshifted component stops increasing at 05:16 as shown in Figure 8.

The strong polarization (about 50%) of the microwave emission continues during the preheating. This fact suggests that the radio emission during the preheating is also due to the thermal plasma. The degree of polarization falls to 20% after 05:14 since the microwaves in this period are mainly due to gyrosynchrotron emission by high-energy electrons. The time behaviour of the polarization is similar to that of the relative velocity and ion temperature of the blueshifted component obtained from Ca xix. The decrease of the relative velocity of the blueshift component indicates thermalization of the plasma.

The density ratios $n(\text{Ca xix})/n(\text{H})$ and $n(\text{Fe xxv})/n(\text{H})$ show a time-dependent history; the values in the rising phase are smaller than those in the decay phase. This indicates nonequilibrium ionization of He-like ions. The ion density ratios of Fe ions, $n(\text{Fe xxiv})/n(\text{Fe xxv})$, $n(\text{Fe xxiii})/n(\text{Fe xxv})$, and $n(\text{Fe xxii})/n(\text{Fe xxv})$, are also shifted from the values in ionization equilibrium indicating ionizing plasmas. The derived value of $n(\text{Fe xxii})/n(\text{Fe xxv})$ is quite small compared to other ion ratios, as shown in Figure 10. This is due to the coincident wavelength of the dielectronic and inner shell satellite line of the B-like Fe ions. We should investigate the wavelengths and rate coefficients more carefully for B-like Fe ion satellite lines.

For the nonequilibrium ionization problem, the effect of the differential emission measure has to be considered. In the rising phase $T_e(\text{Fe})$ and $T_e(\text{Ca})$ are different and indicate a temperature distribution in the flare. However, in the decay phase the derived T_e of two different ions is almost the same. The deviation from ionization equilibrium in the

decay phase cannot be explained by the differential emission measure. In order to explain the observed Fe xxiv–xxii inner shell line intensities with a differential emission measure model, we need a very sharp increase of emission measure for lower temperature which is not realistic. Lemen et al. (1984) considered the effect of the multithermal plasma on the Fe xxii–xxv spectrum and concluded that the effect of the differential emission measure is small. It is justifiable to consider a single-temperature model for the purpose of comparison with the BCS observations.

Feldman (1995) raised a question about steady state coronal ionization equilibrium in the solar upper atmosphere. He showed the examples of discrepancies between ionization equilibrium and observations using the results of the spectroscopic observations. The X-ray spectra in a transient ionizing solar flare plasma within 1 minute at the very early rising phase was considered in Doschek & Tanaka (1987).

Doschek & Feldman (1981) discussed the possible explanation of the enhancement of line q from ionization equilibrium as follows: (1) some contamination of other lines, (2) atomic data, (3) diffusion of ions in flare, (4) charge exchange with neutral hydrogen, (5) high-energy non-thermal electrons. We believe that (3) and (5) are the probable reasons for the deviation. We plan to make a time-dependent ionization model including high-energy electrons and/or the flow in solar flares.

The authors thank K. Shibata, T. Fujimoto and J. Dubau for useful discussions. They are also grateful to A. Sterling for useful information and discussions and to R. More for useful discussion and reading the manuscript. The authors would also like to thank M. Ohira, R. Igaue, and K. Tonomura for spectral fit and graphs. The Mitaka Flare Telescope Group kindly provided us with the magnetograph data.

REFERENCES

- Antonucci, E., Doderio, M. A., Gabriel, A. H., Tanaka, K., & Dubau, J. 1987, *A&A*, 180, 263
- Bely-Dubau, F., Dubau, J., Faucher, P., & Gabriel, A. H. 1982, *MNRAS*, 198, 239
- Bentley, R. D., Doschek, G. A., Simnett, G. M., Rilee, M. L., Mariska, J. T., Culhane, J. L., Kosugi, T., & Watanabe, T. 1994, *ApJ*, 421, L55
- Culhane, J. L., et al. 1992, *PASJ*, 44, L101
- Culhane, J. L., et al. 1994, *Sol. Phys.*, 153, 307
- Doschek, G. A. 1990, *ApJS*, 73, 117
- Doschek, G. A., & Feldman, U. 1981, *ApJ*, 251, 792
- Doschek, G. A., Feldman, U., Kreplin, R. W., & Cohen, L. 1980, *ApJ*, 239, 725
- Doschek, G. A., Mariska, J. T., & Sakao, T. 1996, *ApJ*, 459, 823
- Doschek, G. A., et al. 1994, *ApJ*, 431, 888
- Doschek, G. A., et al. 1992, *PASJ*, 44, L95
- Doschek, G. A., et al. 1993, *ApJ*, 416, 845
- Doschek, G. A., & Tanaka, K. 1987, *ApJ*, 323, 799
- Feldman, U. 1995, *Comments At. Mol. Phys.*, 31, 11
- Fludra, A., et al. 1993, *Adv. Space Res.*, 13, 395
- Fludra, A., Lemen, J. R., Jakimiec, J., Bentley, R. D., & Sylwester, J. 1989, *ApJ*, 344, 991
- Fujimoto, T., & Kato, T. 1984, *Phys. Rev. A*, 30, 379
- Itikawa, Y., Kato, T., & Sakimoto, K. 1995, ISAS Rep. No. 657, Japan
- Kato, T., Masai, K., Sakimoto, K., Itikawa, Y., Watanabe, T., & the BCS Group. 1993, *Proc. 4th Conf. Plasma Physics and Controlled Nuclear Fusion (ESA SP-351)*, 199
- Kato, T., Safronova, U., Shlyaptseva, A., Cornille, M., & Dubau, J. 1997, *At. Data Nucl. Data Tables*, in press.
- Kosugi, T., et al. 1991, *Solar Phys.*, 136, 17
- Lang, J., et al. 1992, *PASJ*, 44, L55
- Lemen, J. R., Phillips, K. J. H., Cowan, R. D., Hata, J., & Grant, I. P. 1984, *A&A*, 135, 313
- Mariska, J. T. 1994, *ApJ*, 434, 756
- Mewe, R., Gronenschild, E. H. B. M., & van den Oord, G. H. J. 1985, *A&AS*, 62, 197
- Mewe, R., Lemen, J. R., & van den Oord, G. H. J. 1986, *A&AS*, 65, 511
- Meyer, J.-P. 1985, *ApJS*, 57, 172
- Nakajima, H., et al. 1994, *IEEE Proc.*, 82, 705
- Sterling, A. C., Doschek, G. A., & Pike, C. D. 1994, *ApJ*, 435, 898
- Sylwester, J., Lemen, J. R., & Mewe, R. 1984, *Nature*, 310, 665
- Tanaka, K. 1986, *PASJ*, 38, 225
- Tsuneta, S., et al. 1991, *Sol. Phys.*, 136, 37